ACSNANO

www.acsnano.org

ARTICLE

Deep-Learning-Based Deconvolution of Mechanical Stimuli with $Ti_3C_2T_x$ MXene Electromagnetic Shield Architecture *via* Dual-Mode Wireless Signal Variation Mechanism

Gun-Hee Lee, Gang San Lee, Junyoung Byun, Jun Chang Yang, Chorom Jang, Seongrak Kim, Hyeonji Kim, Jin-Kwan Park, Ho Jin Lee, Jong-Gwan Yook, Sang Ouk Kim,* and Steve Park*

Cite This: https://dx.doi.org/10.1021/acsnano.0c05105 Read Online

ABSTRACT: Passive component-based soft resonators have been spotlighted in the field of wearable and implantable devices due to their remote operation capability and tunable properties. As the output signal of the resonator-based wireless communication device is given in the form of a vector (*i.e.*, a spectrum of reflection coefficient), multiple information can, in principle, be stored and interpreted. Herein, we introduce a device that can deconvolute mechanical stimuli from a single wireless signal using dual-mode operation, specifically enabled by the use of $Ti_3C_2T_x$ MXene. MXene's strong electromagnetic shielding effect enables the resonator to simultaneously measure pressure and strain without overlapping its output signal, unlike other conductive counterparts that are deficient in shielding ability. Furthermore, convolutional neural-network-based deep learning was implemented to predict the pressure and strain values from unforeseen output wireless signals. Our MXene-integrated wireless device can also be utilized as an on-skin mechanical stimuli sensor for rehabilitation monitoring after orthopedic surgery. The dual-mode signal variation mechanism enabled by integration of MXene allows wireless communication systems to efficiently handle various information simultaneously, through which multistimuli sensing capability can be imparted into passive component-based wearable and implantable electrical devices.

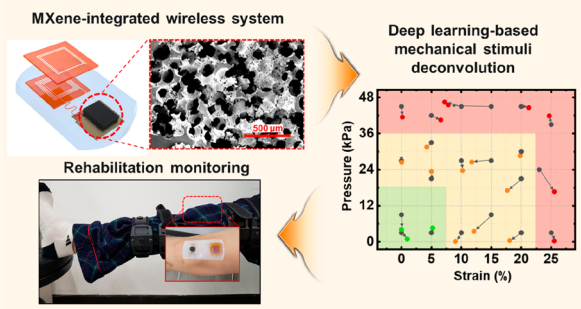

KEYWORDS: *mechanical stimuli deconvolution, MXenes, wireless communication, deep learning, rehabilitation monitoring, tactile sensors, LC resonator*

Wireless communication systems have received a great deal of interest in recent years due to their importance for health monitoring in wearable and implantable electronics.[1−3] In particular, soft, functional material-based passive wireless devices have been spotlighted owing to their tunable properties for various applications (*e.g.*, a biodegradable material-based resonator can be used for transient implantable electronics, while a self-healing materials-based resonator can be used for adaptable e-skin).[4−9] One notable, however, not widely utilized characteristic of a passive LC resonator-based wireless communication system is storing and processing of multiple information simultaneously. As the output signal acquired from an LC resonator is represented as a 2D spectrum with a resonance peak (*i.e.*, reflection coefficient according to frequency), monitoring two types of variations with a single signal can, in principle, be implemented based on a dual-mode signal variation mechanism.[6,7,10] Specifically, the resonance peak of the reflection coefficient (S_{11}) can be varied along the horizontal or vertical axis, depending on the operating mode. For instance, if the quality factor of the LC resonator changes, the magnitude of the resonance peak changes. On the other hand, if inductance or capacitance of the LC resonator changes, the resonant frequency changes. Thus far, conventional resonator-based wireless communication systems have been relying on one or the other operating

Received: June 19, 2020
Accepted: August 19, 2020
Published: August 19, 2020

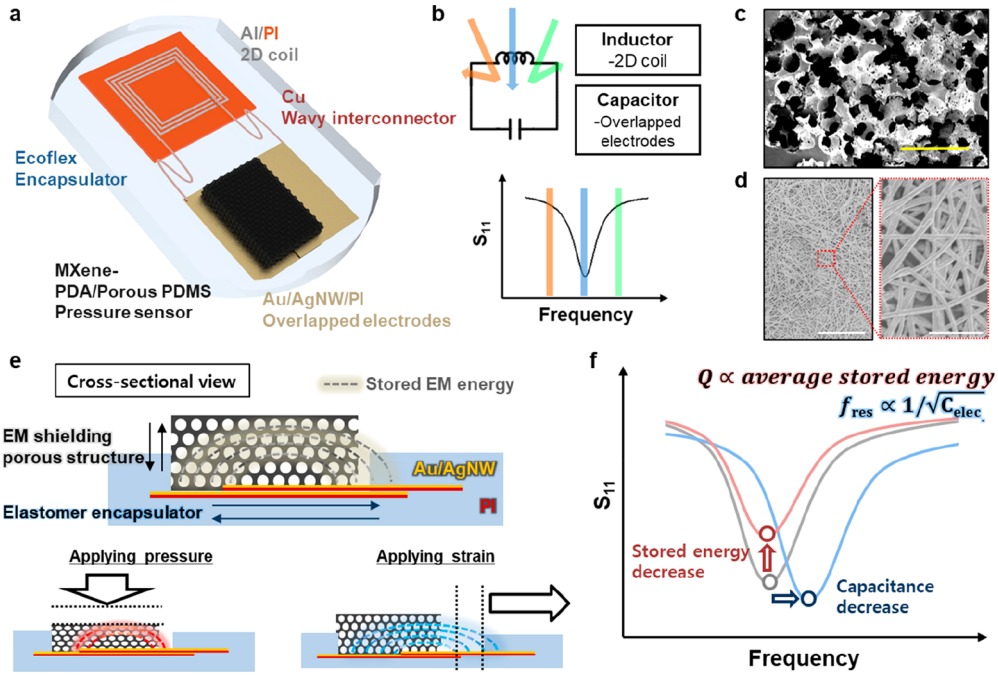

Figure 1. Device structure and sensing mechanism of MXene-based wireless sensing platform capable of differentiating pressure and strain (MXWiDi). (a) Schematic depiction of MXWiDi composed of 2D coil, flexible overlapped electrodes, and MXene-coated porous pressure sensor. (b) Equivalent circuit of MXWiDi and conceptual depiction of the closed LC resonator with a specific resonant frequency. (c) SEM image of MXene-coated porous PDMS (scale bar: 500 μm). (d) SEM image of Au-coated AgNWs on PI film (scale bar: 5 and 1 μm, respectively). (e) Schematic illustration of cross-sectional view across the pressure sensor and overlapped electrodes when each mechanical stimuli is applied. (f) Conceptual depiction of S_{11} spectrum variation according to the change in the capacitance between the electrodes and the stored energy in the LC resonator.

modes, and a dual-mode signal variation mechanism was rarely implemented due to a lack of comprehensive understanding of the signal variation mechanism related to material properties and device structure.[1−4,6]

Dual-mode signal acquisition can be critically important in tactile sensing applications, particularly in regards to the simultaneous measurement and decoupling of pressure and strain.[11−15] For instance, in wearable electronics, differentiation of strain and pressure is required to accurately monitor body motion and vital signals without interference.[3] In robotics, distinguishing of strain and pressure is essential to properly carry out complex tasks such as handling and manipulating objects.[12,13] In the case of an implantable device where it is burdensome to put in multiple sensors in the human body, it is practically required for a single sensor to measure multiple stimuli.[16] However, an effective mechanical stimuli decoupling strategy using a single output signal by means of a single device still remains a formidable challenge. The origin of hardship in differentiating pressure and strain is the inherent mechanical coupling of the two stimuli by Poisson's ratio (*i.e.*, the pressure applied to material causes strain and *vice versa*).[3,17] To cope with this matter, researchers have exploited several alternative strategies. Concurrent analysis of many output signals can decouple pressure and strain.[16,18−20] However, such a strategy complicates the measurement circuitry and wiring. Another common way is to deploy multiple sensors, each of which respond to only one kind of stimuli. Nonetheless, the need for multiple sensors complicates the fabrication and integration process and inevitably yields multiple signals.[21−23] Furthermore, the tethered operation of the wire-based system hinders its practical use in the wearable and implantable devices for healthcare monitoring.

In this work, we report a MXene-integrated wireless sensing platform capable of differentiating pressure and strain (MXWiDi) by deconvoluting a single signal output *via* a dual-mode wireless signal variation mechanism. Here, deconvolution refers to resolving the constituents (*i.e.*, pressure and strain) that determine the shape of the signal output. This technology was enabled specifically by the use of $Ti_3C_2T_x$ MXene. MXenes are emerging 2D materials that have been receiving a great deal of interest in recent years, particularly owing to their high electromagnetic (EM) shielding effect.[24,25] This feature has been attributed to the intrinsic high electrical conductivity of each flake, multiple internal reflections within a layered structure, and the attenuation of EM radiation at abundant polar surface functionalities.[24] These properties result in an ultrahigh dielectric constant on the order of 10^5 when MXenes are mixed with insulating polymers.[26] The EM shielding effect can potentially be advantageously utilized in LC resonator-based wireless tactile sensors; however, such a demonstration has not yet been reported. Herein, coating MXene on a porous elastomer with the polydopamine (PDA) adhesive layer enabled stable and reliable operation. Unlike other conductive counterparts, such as polypyrrole (Ppy), MXene's superior electromagnetic shielding ability yielded a unique spectrum at various combinations of pressure and strain. Subsequently, convolutional neural-network-based deep learning was implemented for the regression of the trained reflection coefficient spectrum and the prediction of the untrained spectrum. Finally, as a proof of concept, MXWiDi was employed in rehabilitation monitoring after orthopedic surgery, demonstrating the potential of the wireless multi-

https://dx.doi.org/10.1021/acsnano.0c05105
ACS Nano XXXX, XXX, XXX−XXX

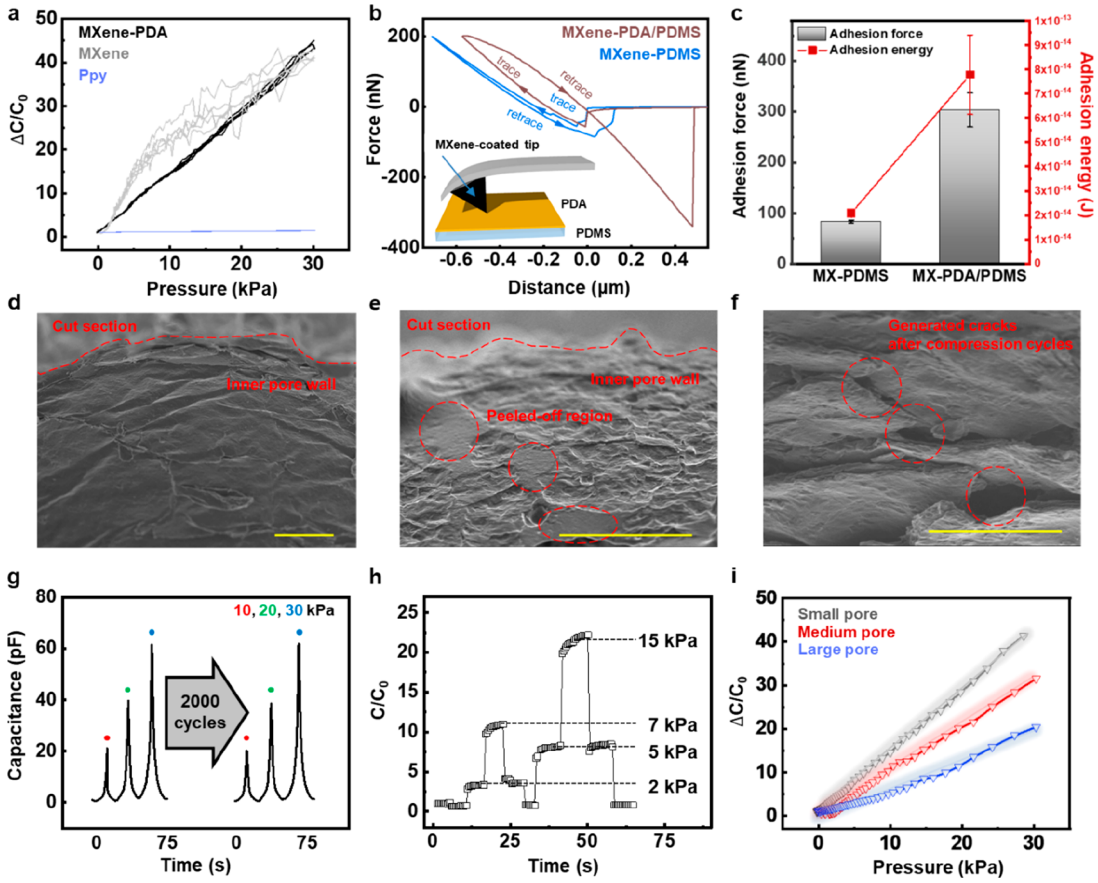

Figure 2. MXene-coated porous PDMS for pressure sensing. (a) Relative capacitance variation as a function of pressure for each coating material. (b) AFM pull-off tests between MXene-coated tip and PDMS surface with/without PDA adhesive layer. (c) Adhesion force and energy of MXene-PDMS and MXene-PDA/PDMS at 10 random positions. (d) Cross-sectional SEM image of MXene-coated PDMS with the PDA adhesive layer. (e,f) Cross-sectional SEM image of MXene coated on PDMS without the PDA adhesive layer. Several peeled-off regions (e) and cracks (f) are observed on the inner pore wall (yellow scale bar represents 10 μm). (g) Capacitance variation according to compression and release cycling of MXene-coated porous PDMS with PDA adhesive layer. (h) Continuous monitoring of capacitance under applying discrete pressure levels. (i) Relative capacitance of porous PDMS with different pores size under applied pressure.

stimuli deconvolution system as a possible candidate for biomedical engineering.

RESULTS AND DISCUSSION

Overall Device Structure and Sensing Mechanism of MXWiDi. Figure 1a is the overall schematic of MXWiDi, consisting of a closed-loop LC resonator (which comprises an inductor (2D coil) and a capacitor (overlapped electrodes)) and MXene-coated porous polydimethylsiloxane (PDMS) elastomer placed on top of the overlapped electrodes. The LC resonator has a specific EM wave frequency that it stores, which results in a specific resonance peak (*i.e.*, a sharp decrease in S_{11} at a given frequency) in the S_{11} spectrum, as depicted in Figure 1b.[6,10] Figure S1 is the schematic of the MXWiDi fabrication process (further details of the fabrication process are described in the Materials and Methods section). First, Al was thermally deposited on top of polyimide (PI) film using shadow masking to generate the 2D coil (see Figure S2 for the fabrication process). Two electrodes were fabricated by coating Ag nanowires (NWs) on top of PI films, followed by the deposition of the Au layer. The two electrodes were vertically stacked with a lateral offset to form overlapped electrodes. The 2D coil and the overlapped electrodes were placed on an Ecoflex elastomer substrate (*i.e.*, bottom elastomer). The electrodes and the 2D coil were electrically connected using Cu wavy interconnects, which allows stable operation under strain (see Figure S3 for strain distribution simulation of the wavy interconnects). Thereafter, another layer of Ecoflex (*i.e.*, top elastomer) was placed over the bottom elastomer as a means to encapsulate and securely anchor the 2D coil and the overlapped electrodes. In particular, the top elastomer was designed to partially cover the overlapped electrodes so that only the ends of the electrodes were anchored (*i.e.*, the bottom electrode anchored on the left end and the top electrode anchored on the right end; see Figure S4 for fabrication detail). This enables the electrodes to slide laterally in response to the applied strain. Finally, MXene-coated porous PDMS was placed on top of the overlapped electrodes, anchored to one sidewall of the top elastomer to remove the Poisson effect on the porous PDMS caused by lateral strain on the electrodes.

Figure 1c is the SEM (scanning electron microscopy) image of the MXene-coated PDMS porous structure. To strongly adhere MXene on the PDMS surface, PDA was used as an interfacial adhesive layer (see Figures S5 and S6 for the fabrication process). Figure 1d shows the SEM images of the Au-coated AgNW film, which show high density of NWs on the surface. Au coating was critical to ensure high conductivity and stable binding of AgNWs to the PI surface. Without Au coating, the AgNWs were easily rubbed off of the PI surface, significantly degrading their durability during operation

https://dx.doi.org/10.1021/acsnano.0c05105
ACS Nano XXXX, XXX, XXX−XXX

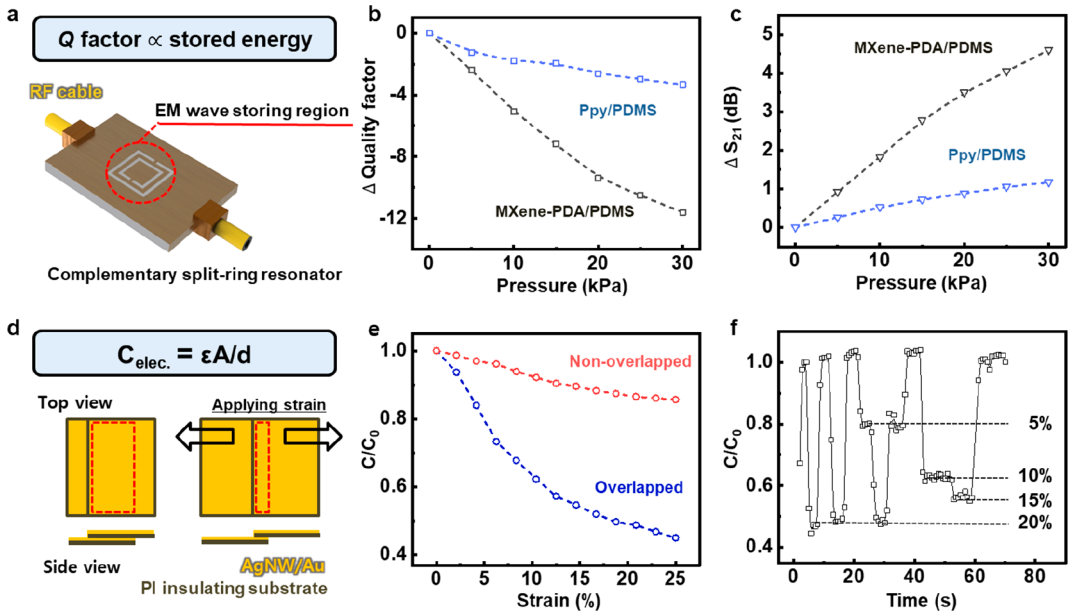

Figure 3. Pressure and strain sensing characterization in a wired system. (a) Schematic depiction of electromagnetic wave-shielding-based pressure sensing mechanism in complementary split-ring resonator (CSRR). (b) Variation of quality factor of CSRR as a function of pressure for each type of coating material. (c) Variation of the S_{21} peak magnitude as a function of pressure for each type of coating material. (d) Schematic depiction of overlapped area variation-based strain sensing mechanism. (e) Relative capacitance as a function of strain for overlapped and non-overlapped electrodes. (f) Continuous monitoring of capacitance under discrete strain levels.

(Figure S7 shows SEM images of the AgNW and Au-coated AgNW films after repeated application of pressure).[27]

Figure 1e is the cross-sectional view of the overlapped electrodes with MXene-coated porous elastomer on top. The dashed semicircular lines above the overlapped electrodes represent stored EM energy between the two electrodes.[6,10] When pressure is applied to the MXene-coated porous elastomer, the volume proportion of MXene near the electrodes increases, which decreases the stored EM wave between the electrodes. The quality (Q) factor of the LC resonator is proportional to the stored EM energy, as seen in the following equation.[10]

$$Q\,\text{factor} \propto \frac{\text{average stored energy}}{\text{energy loss/second}} \tag{1}$$

Hence, the quality factor decreases with pressure, and this manifests as an increase in the S_{11} peak, as depicted by the red curve of Figure 1f (see Figure S8a for simulation results).

When strain is applied, the overlapping area of the electrodes decreases, resulting in the decrease in capacitance of the LC resonator. The capacitance of the LC resonator and the resonant frequency (f_{res}) are related by the following equation.[10]

$$f_{res} \propto \frac{1}{\sqrt{L_{2Dcoil}C_{elec}}} \tag{2}$$

Here, f_{res} is the resonant frequency, L_{2Dcoil} is the inductance of the 2D coil, and C_{elec} is the capacitance of the overlapping electrodes. Hence, applied strain shifts the S_{11} peak to the right as depicted in the skyblue curve in Figure 1f (see Figure S8 for simulation results). In this manner, pressure and strain can be differentiated.

MXene-Coated Porous PDMS for Pressure Sensing. Prior to the implementation of MXene on a LC resonator, the effect of MXene as a capacitive sensor was analyzed. Considering the high dielectric constant of the MXene composite, it is a promising candidate for a capacitive sensor. Figure S9 is a schematic depiction of an effective dielectric constant variation-based capacitance sensing platform, where the MXene-coated porous PDMS elastomer was placed over laterally patterned electrodes. Upon the application of pressure, the effective dielectric constant of the porous structure increases due to the increase in volume proportion of MXene within the fringe field, which results in an increase in capacitance. Figure 2a is a plot of relative capacitance change *versus* pressure for porous PDMS elastomers coated with MXene (with or without PDA) and Ppy. For each type of sensor, the measurement was repeated five times. Ppy is a conductive polymer that was used previously in pressure sensors owing to its strong adhesion to the PDMS surface and relatively large dielectric constant of ∼10.[6,28] However, compared to MXene-coated counterparts, the sensitivity of Ppy-coated porous PDMS was much lower, owing to the much higher dielectric constant of MXene/polymer composites (Figure S10 is a rescaled plot of Ppy-coated porous PDMS capacitive sensor). The MXene-coated sensor without PDA yielded unstable signal with pressure, presumably due to the poor interfacial adhesion between MXene and the PDMS surface that causes delamination of MXene during repeated compression and release. In contrast, the MXene-coated sensor with a PDA adhesive layer exhibited stable and repeatable sensing performance.

To investigate the origin of the stable operation with a PDA layer, we conducted precise nanoscale adhesion test. Figure 2b represents atomic force microscopy (AFM) pull-off tests between the MXene-coated tip (SEM image of MXene-coated tip is presented in Figure S11) and PDMS surfaces with and without a PDA adhesive layer. Figure 2c shows adhesion force and energy between MXene and PDMS, which shows about a 3-fold increase in the presence of the PDA adhesive layer.[29,30] Figure 2d is a cross-sectional SEM image of the MXene-coated

https://dx.doi.org/10.1021/acsnano.0c05105
ACS Nano XXXX, XXX, XXX−XXX

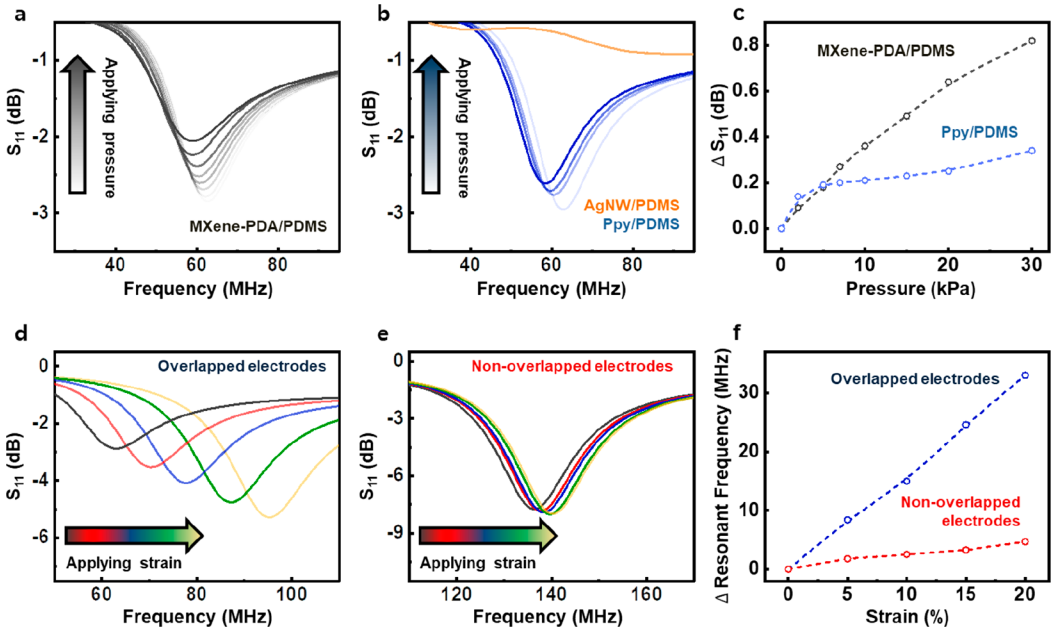

Figure 4. Pressure and strain sensing characterization in a wireless system. (a) S_{11} peak variation of a MXene-coated pressure sensor under different pressure levels. (b) S_{11} peak variation of AgNW- and Ppy-coated pressure sensors under different pressure levels. (c) Variation of the S_{11} peak magnitude as a function of pressure for each type of coating material. (d) S_{11} peak variation of overlapped electrodes under different strain levels. (e) S_{11} peak variation of non-overlapped electrodes under different strain levels. (f) Variation of the resonant frequency as a function of strain for each type of electrode configuration.

PDMS surface with the PDA adhesive layer after 2000 compression cycles, demonstrating that MXene flakes are still intimately attached. In contrast, the MXene-coated PDMS surface without the PDA adhesive layer shows delamination and crack generation, which results in unstable operation during compression and release (Figure 2e,f). Figure 2g is the capacitance variation of MXene-coated porous PDMS with PDA adhesive under compression and release. As MXene adhered well to the porous elastomer surface, it exhibited little hysteresis and operated stably over 2000 cycles. Figure 2h presents the relative capacitance change versus time under discrete pressure levels, which verifies the reliability of sensing. Relative capacitance change under continuous loading and unloading of pressure is available in Figure S12. For the rest of this study, the MXene-coated sensor with a PDA adhesive layer was used.

Using microfluidic channels with different diameters, porous PDMS with various pore sizes can be fabricated, through which sensitivity of the pressure sensor can be tuned (Figure S13).[31] Figure 2i is a plot of relative capacitance change as a function of pressure for porous PDMS with different pore sizes (100, 200, and 500 μm). The porous PDMS with the smallest pores had the highest sensitivity (1.39 kPa^{-1}), which can be attributed to its highest surface to volume ratio; the application of pressure yields a larger increase in the effective dielectric constant between the two lateral electrodes. We also observed the relatively linear behavior of sensors with R^2 in the range of 0.986−0.999. Further discussion about linearity is in Figure S14.

Dual Mechanism Analysis in a Wired System. As depicted in Figure 3a, EM energy in the form of an electric field is concentrated at the center of the complementary split-ring resonator (CSRR).[32] After placing MXene-coated and Ppy-coated porous PDMS inside the ring of the CSRR, we monitored the variation of stored EM energy under different pressure levels. As shown in Figure 3b, when the proportion of MXene near the ring increases according to pressure, stored EM energy is decreased due to the EM shielding effect of MXene, resulting in the decrease in the quality (Q) factor of CSRR. As MXene's EM radiation shielding effect is superior compared to that of counterpart materials, the reduction of stored EM energy is higher. The decrease in the quality factor results in the increase in the transmission coefficient (S_{21}) of the resonance peak. The S_{21} peak of the MXene-based sensor increases more than that in Ppy-based sensors (Figure 3c), which further verifies the superior shielding effect of MXene and its feasibility as an LC resonator-based pressure sensor.

Figure 3d is a schematic depiction of how the strain was measured using overlapped electrode geometry. Under strain, the overlapped area (A) decreases, which reduces the capacitance. Figure 3e is a plot of relative capacitance change *versus* strain for overlapped and non-overlapped electrodes. The overlapped electrode configuration was more sensitive compared to that of non-overlapped electrodes, as the change in the overlapped area brings forth a greater change in the capacitance than the change in the lateral distance between two electrodes. Figure 3f is a plot of relative capacitance change *versus* time under various strain levels for the overlapped electrodes, showing stable sensing performance. Relative capacitance change under continuous loading and unloading of strain is available in Figure S15.

Dual Mechanism Analysis in a Wireless System. The MXene-coated PDMS sensor was placed on top of the overlapping electrodes of the LC resonator, and the S_{11} spectra were attained at different pressure levels up to 30 kPa (Figure 4a). Here, porous PDMS with large pores was used due to its large sensing range, as opposed to porous PDMS with small pores, which had higher sensitivity but smaller sensing range (Figure S16). With increasing pressure, the S_{11} peak gradually increases. This can be attributed to the reduction of stored EM

https://dx.doi.org/10.1021/acsnano.0c05105
ACS Nano XXXX, XXX, XXX−XXX

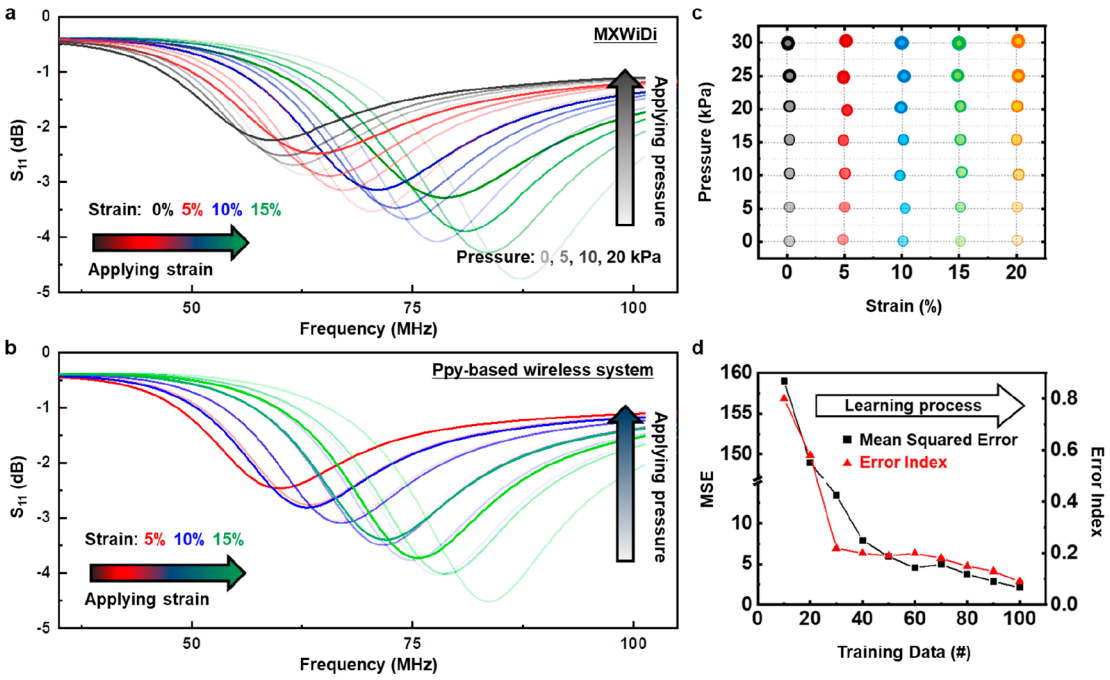

Figure 5. Deconvolution of pressure and strain in a wireless system. (a) Output S_{11} spectrum of MXWiDi according to given pressure and strain. All spectra are not overlapped with each other. (b) Output S_{11} spectrum of Ppy-coated porous PDMS pressure sensor-based wireless system according to various pressures and strains. (c) Regression of output S_{11} spectrum at various pressure and strain combinations using MXWiDi. (d) Mean squared error (MSE) and the error index according to the number of training data in the MXWiDi-based platform.

energy, yielding a decrease in quality factor, as mentioned above. Figure 4b is the S_{11} spectra under different pressure levels applied to porous PDMS coated with Ppy and AgNWs. As a AgNW is a metal with high conductivity, pressure levels could not be measured as the two electrodes shorted even at a very low pressure of 0.5 kPa. For Ppy, due to its comparatively inferior EM shielding effect, the change in the S_{11} peak with pressure was relatively small. Figure 4c is a plot of change in the S_{11} peak *versus* pressure for MXene- and PPy-coated porous PDMS, showing the relatively high sensitivity for the MXene-coated sample. Under repeated loading and unloading of 30 kPa pressure, the MXene-coated porous PDMS with PDA adhesive layer shows a stable pressure monitoring capability in the wireless system, as shown in Figure S17.

Looking closely at Figure 4a, along with the increase in S_{11} peak, there is a slight leftward shift in the resonant frequency with applied pressure. As discussed in Figures 2a, the increase in volume fraction of MXene with pressure also increases the effective dielectric constant and, consequently, the capacitance of the LC resonator. The increase in the capacitance of the LC resonator also increases the S_{11} peak, as explained in Figure S18.[6] Therefore, resonant frequency and the magnitude of S_{11} peak are not completely independent of each other. Despite the interdependence, due to the strong EM radiation shielding effect of MXene, the change in the stored EM radiation with pressure is a more dominant effect. As will be discussed later, this generates a unique S_{11} spectrum at a given pressure and strain. In the case of Ppy, with a relatively low EM radiation shielding effect, the change in the capacitance of the LC resonator with pressure is a more dominant effect. In other words, using Ppy, the change in the S_{11} spectrum with the application of pressure would overlap with that of the application of strain (which also changes the capacitance of the LC resonator).

Figure 4d presents the S_{11} spectra at various strains, exhibiting that the resonant frequency shifts to the right with increasing strain due to the decrease in the capacitance of LC resonator. Figure 4e is the S_{11} spectra at various strains for non-overlapped electrodes, which show that the shift in resonant frequency is insignificant as the change in the capacitance of the LC resonator is minimal. Figure 4f is a plot of resonant frequency shift as a function of strain, demonstrating that the overlapped electrode configuration is more sensitive compared to that of the non-overlapped counterpart. Under repeated 20% stretching and releasing, the overlapped electrodes show a stable strain monitoring capability in the wireless system, as shown in Figure S19.

Deconvolution of Mechanical Stimuli *via* Single Wireless Signal. Figure 5a is the S_{11} spectra for MXWiDi under the simultaneous application of various combinations of pressure and strain. The color represents different strain levels, and brightness represents different pressure levels. At various combinations, a unique S_{11} spectrum was generated, through which pressure and strain can be deconvoluted. As mentioned above, under the application of pressure, the S_{11} peak sharply increases due to the strong EM radiation shielding effect of MXene, which prevents the S_{11} spectra from overlapping. On the other hand, for the Ppy-based pressure sensor, the relatively weak EM shielding effect renders deconvolution in the wireless system impractical, as seen in Figure 5b.

The S_{11} spectrum can be thought of as a vector (*i.e.*, a list of S_{11} values at different frequencies) that contains pressure and strain information. Hence, in order to extract and quantify pressure and strain information from a given S_{11} spectrum, convolutional neural-network (CNN)-based deep learning for regression and prediction was implemented (network architecture is presented in Figure S20).[33,34] First, utilizing CNN-based regression, 35 S_{11} spectra at various pressure and strains were used as input training data. Thereafter, S_{11} spectra

https://dx.doi.org/10.1021/acsnano.0c05105
ACS Nano XXXX, XXX, XXX−XXX

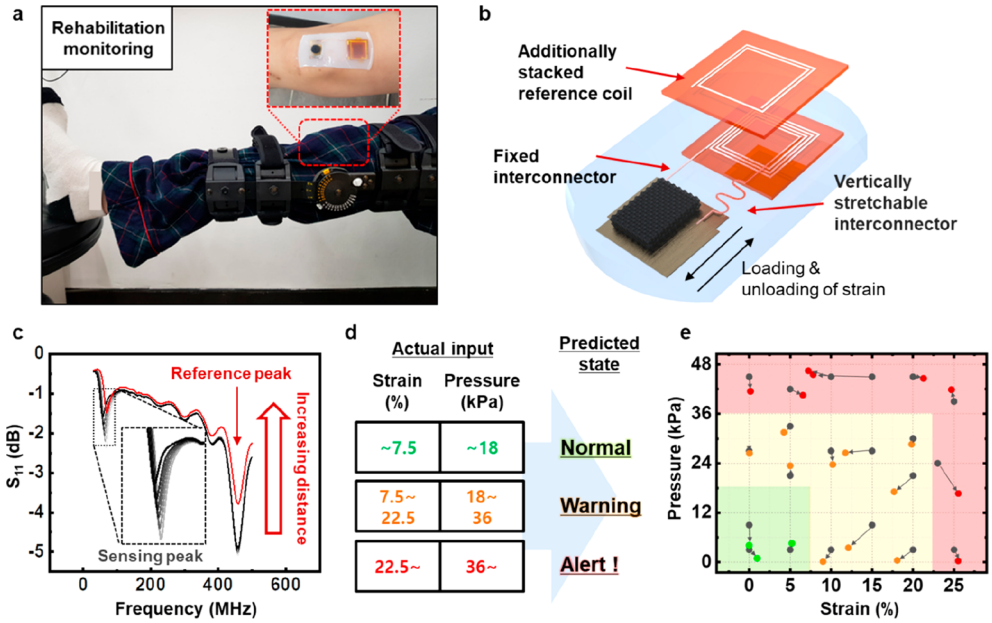

Figure 6. Application of MXWiDi for rehabilitation monitoring. (a) Photograph of MXWiDi mounted on a human knee for rehabilitation monitoring after orthopedic surgery. (b) Schematic illustration of modified MXWiDi for rehabilitation monitoring application. (c) S_{11} spectra of MXWiDi, including sensing peak and reference peak. (d) Schematic depiction of mechanical stimuli categorization according to pressure and strain. (e) Visualization plot comparing the actual mechanical information (dark gray) and predicted one.

were attained again at the same combinations of pressure and strain, which was used as test data to determine the predicting accuracy. Figure 5c represents a pressure *versus* strain map where the different colors and brightness represent strain and pressure levels, respectively. Different sets of pressure and strain values were predicted with a low error index of 0.02. Error index is defined as follows:

$$\text{Error Index} = \frac{1}{N}\sum \frac{|M_{\text{pred},i} - M_{\text{act},i}|}{|M_{\text{act},i}|}, \quad i \in \{1, 2, \ldots N\} \tag{3}$$

where $M_{\text{pred.i}}$ and $M_{\text{act.i}}$ are the expected and actual values of the applied pressure and strain in vector form (*i.e.*, M_{pred} or $M_{\text{act}} = \langle P,S \rangle$, where P is the pressure and S is the strain applied). This result verifies that each S_{11} spectrum is unique to a given set of pressure and strain.

To confirm whether pressure and strain can be predicted from an untrained input data, CNN-based deep learning was implemented (Figure 5d). After training with 100 data, 25 test data were used to verify the accuracy of the deeplearning algorithm. The mean squared error and error index were 2.12 and 0.09, respectively, which are adequately low, indicating the usefulness of combining MXWiDi with deep learning algorithm to deconvolute and predict unforeseen pressure and strain levels. Predicted output values after training with 100 data are presented in Figure S21.

Rehabilitation Monitoring Application. MXWiDi's biocompatibility, softness, light-weight, untethered operation, and differentiation capability render it ideal for health monitoring applications. Figure 6 presents a demonstration of MXWiDi in rehabilitation monitoring. After orthopedic surgery, a painkiller is generally injected in the surgically repaired area to alleviate pain. Unfortunately, the painkiller renders the patient insensitive to mechanical stimuli, making them more susceptible to further injury. For rehabilitation monitoring, differentiation of pressure and strain is important to accurately determine the potential danger of injury for each stimuli.[16,35] Figure 6a is a photograph of MXWiDi on top of the subject's knee and thigh. The communication part (*i.e.*, 2D coil) and the sensing part of our device are spatially separated. Therefore, the 2D coil can be placed on the region where only slight mechanical deformation occurs (thigh) for the stable wireless communication, whereas the sensing part can be placed where mechanical deformation is concentrated (knee). Figure 6b is a schematic illustration of the newly designed MXWiDi, with an additional reference coil that generates an additional reference peak. Further discussion about stacked-coil design is presented in Figure S22. The reference peak was designed to only change with the distance between the 2D coil and the reader, through which S_{11} spectra can be calibrated (*i.e.*, as the magnitude of S_{11} spectra can change with the distance between 2D coil and reader, pressure cannot be accurately measured when the distance changes).[6,36] Figure 6c shows the S_{11} spectra under different pressure levels with the aforementioned reference peak. The red curve indicates the S_{11} spectrum at a higher distance between the 2D coil and the reader. By adopting the reference peak, both the distance and angle between the coil and the reader can be calibrated (Figure S23). For this demonstration, CNN-based deep learning was conducted once again, where only 30 training data (S_{11} spectra at various pressure and strains) were used to train the system to verify its practical use. Here, rather than predicting the actual pressure and strain values, the focus was to classify a given pressure and strain value into three categories: normal, warning, and alert with the relatively small number of training data. Figure 6d is a schematic depiction of the boundary values of strain and pressure that were used to divide each category and the corresponding output predictions. Figure 6e is a pressure *versus* strain map where black dots represent actual pressure and strain values, whereas the green, orange, and red dots indicate predicted pressure and strain values within the three categories. Although the exact pressure and strain values

https://dx.doi.org/10.1021/acsnano.0c05105
ACS Nano XXXX, XXX, XXX−XXX

were not accurately predicted, it nevertheless correctly classified the input data into the three categories. If the number of training data increases, prediction accuracy is also enhanced, as shown in Figure S24.

CONCLUSIONS

In this work, we introduced MXWiDi, a single-device-based, soft wireless sensing platform that can deconvolute pressure and strain inputs from a single signal output. MXene's superior electromagnetic shielding effect resulted in a decrease in the stored EM energy in the LC resonator upon the application of mechanical pressure and thereby yielded a distinct increase in the S_{11} peak. By contrast, application of strain resulted in a decrease in the capacitance of the LC resonator, increasing the resonant frequency. For various combinations of pressure and strain values, unique S_{11} spectra were attained. Using CNN-based deep learning, pressure and strain values were predicted with a mean squared error and error index of 2.12 and 0.09, respectively. We also demonstrated that an intimate adhesion between MXene and PDMS in the presence of a PDA adhesive layer results in not only stability but also high linearity and tunable sensitivity in capacitive sensing. This presents the possibility of various pressure sensing applications using MXene.[3,37,38] Finally, MXWiDi was utilized as an on-skin rehabilitation monitoring system with the "reader on textile" concept,[7,8,39] where pressure and strain applied to a subject were classified. We project that these demonstrations will be the fundamental groundwork for various wireless tactile sensing applications in wearable and implantable electronics in the future.

MATERIALS AND METHODS

Fabrication of Porous PDMS. The perfluoroalkoxyalkane tube-based (outer and inner diameters are 1 mm and 500 μm, respectively) microfluidic channel connected with the T-shape connector. The hole size of the T-shape connector determined the pore size of porous PDMS. The PDMS (K1 solution, Republic of Korea) was mixed with hexadecane (Sigma-Aldrich) and span80 (surfactant, Sigma-Aldrich). The weight ratio of three components (PDMS, hexadecane, span80) in mixed PDMS oil was 1.05:1:0.04. The flow rate between mixed PDMS oil and deionized water was 4:1. Pumping speed was controlled by the syringe pump (Harvard Apparatus). The PDMS oil containing an emulsion water droplet was accumulated into a glass mold and cured under 90 °C for 12 h. Through curing, the water droplet was evaporated; subsequently, the pore structure in PMDS was fabricated. A schematic illustration of this step is presented in Figure S5.

MXene Synthesis. Following the well-established minimally intensive layer delamination method, 4.8 g of LiF (Alfa Aesar) was dissolved in 60 mL of 9 M HCl solution.[25] After sufficient time for dissolution, 3 g of Ti_3AlC_2 powder (Carbon-Ukraine Ltd.) was added slowly to the LiF/HCl solution. The addition process should be slow enough to avoid a sudden temperature increase of the solution due to the exothermic reaction. The etching process was taken for 24 h with 200 rpm magnetic stirring at 35 °C. As illustrated in Figure S6a, the Al layer was selectively etched out by evolved HF in this step. The resultant solution was washed 2−3 times with deionized water by repeated centrifugation (3500 rpm) and decanting. During this process, $Ti_3C_2T_x$ MXene flakes were delaminated and dispersed in the water. When the supernatant showed a pH of 5−6, the $Ti_3C_2T_x$ aqueous solution was collected from the supernatant after centrifugation at 3500 rpm to remove unreacted Ti_3AlC_2.

MXene Coating on Porous PDMS. Porous PDMS was treated with O_2 plasma to make the surface hydrophilic. Subsequently, it is soaked to PDA coating solution prepared by dissolving 20 mg of dopamine hydrochloride (Sigma-Aldrich) in 10 mM Tris-HCl buffer solution (pH 8.5). After 30 min, the PDMS template was mildly rinsed with deionized water, followed by immersion into an as-synthesized $Ti_3C_2T_x$ aqueous solution of 10 mg/mL for 5 h. Finally, MXene-PDA/porous PDMS was prepared after being dried in air. A MXene-coated PDMS control sample was prepared the same without the PDA coating step. A schematic illustration of this step is presented in Figure S6b.

Fabrication of 2D Coil. The surface of the PI film was cleaned using O_2 plasma (50 W, 1 min). The four-turns 2D coil was composed of aluminum. First, all of the horizontal components of the coil were thermally vacuum-deposited about 150 nm using a shadow mask. The second layer of metal for the vertical component of coils was deposited at 250 nm after aligning the mask to the feature of the horizontal metal layer. The additional PI tape was laminated on the 2D coil for insulation and encapsulation. This PI tape had the hole for electrical conductivity, which was cut by a razor blade. A schematic illustration of this step is presented in Figure S2.

Fabrication of Flexible Electrodes. PI film was cut with a dimension of PI at 1.5 cm × 2.5 cm using a laser cutter (Epilog Fusion M2 Laser, Epilog Laser). The surface of PI was prepared by applying O_2 plasma (50 W, 1 min) for solution-based coating. Subsequently, a 1 wt % solution of silver nanowire was spray-coated on the preheated PI film (at 120 °C by being placed on a hot plate). After being spray-coated, about 200 nm of gold film was thermally deposited on the nanowire-coated PI film.

Mechanical Stimuli Measurement Using Wired Platform. Lateral electrodes were fabricated by thermal deposition of aluminum on a slide glass substrate using a metal mask. MXene- and Ppy-coated porous PDMS was placed on the lateral electrodes. The force gauge (the maximum force is 10 N, Mark-10) which was connected with a motor (a strain rate of 30 mm/min, Mark-10) on the stand was utilized for applying pressure. The capacitance between two lateral electrodes was measured using a LCR meter (4284A, HP). A manual strain machine was used to apply strain. The capacitance variation of two overlapped electrodes was measured using the same LCR meter, which was used to monitor pressure.

MXene-coated AFM Tip Preparation. For a nanoscale adhesion test, we prepared a MXene-coated AFM tip. The as-purchased LFMR AFM tip (Nanosensors) was first coated with the PDA layer following a conventional dip-coating method using a 2 mg mL^{-1} dopamine hydrochloride (Sigma-Aldrich) in 10 mM Tris-HCl buffer solution (pH 8.5). Subsequently, the tip was dipped in 10 mg mL^{-1} of MXene aqueous solution quickly and dried in air.

AFM Adhesion Test. An AFM adhesion test was conducted by contact-mode AFM (XE-100, Park Systems, Republic of Korea). The PDMS substrate was dip-coated with the aforementioned PDA coating solution and measured right after it was taken out. For comparison, bare PDMS was also immersed in deionized water before measurement. We can evaluate adhesion force between the MXene-coated tip and the substrate in wet conditions. AFM was calibrated by force constant and sensitivity of the tip, and the force limit was set at 200 nN. Over 10 random points were measured, and the results are summarized in Figure 2c.

Mechanical Stimuli Measurement Using MXWiDi. Wireless measurement was demonstrated at a frequency range of 1−200 MHz with vector network analyzer (ZND, Rohde & Schwarz). The VNA was connected with a commercial magnetic field reader (HZ-15 RSH400-1, Rohde & Schwarz) through a RF cable. This reader transmitted the magnetic field to the 2D coil at a distance of 5 mm. The LC resonator stored the EM field that matched to its specific resonant frequency, which was shown as sharp decrease in the S_{11} peak. Variation of resonant frequency and magnitude of the S_{11} peak due to strain and pressure was observed. The strain was applied using a manual strain machine, and the pressure was applied using calibration weights.

Convolutional Neural-Network-Based Deep Learning. A total of 125 S_{11} signal data were collected from the stretched sensors under various combinations of pressures and strains. Among all of the data, 25 randomly selected data were assigned as the test set. The input signal was a one-dimensional array of 301 elements. The

https://dx.doi.org/10.1021/acsnano.0c05105
ACS Nano XXXX, XXX, XXX−XXX

network was trained for 2000 steps using an SGD momentum optimizer with the momentum of 0.9, with a fixed learning rate (1×10^{-4}) and weight decay (1×10^{-4}). For each iteration, the entire training set was used as a batch. We designed the network with reference to the VGG-16 network, which is a well-known CNN in the field of computer vision. In addition to the baseline model, index information (*i.e.*, 0, 1, 2, ..., 300) was concatenated with an input signal to make the CNN look different at each position in the signal. The network architecture used in our experiments is illustrated in Figure S16. We set the size of all convolution filters as 3. Lastly, the sigmoid activation at the end of the network was used to limit the output pressure.

SEM Characterization. Scanning electron microscopy measurements were performed using a Hitachi S-4800 (FET) instrument. Osmium was coated on the surface of samples before SEM measurement for clear imaging.

ASSOCIATED CONTENT

Supporting Information

The Supporting Information is available free of charge at https://pubs.acs.org/doi/10.1021/acsnano.0c05105.

Figures S1−S24: schematic illustration of overall fabrication process of MXWiDi; schematic illustration of two-step deposition for fabrication of 2D coil; visualized simulation of strain distribution; schematic illustration of anchoring for strain sensing; schematic illustration of porous PDMS fabrication using microfluidic channel; schematic illustration of MXene coating on porous PDMS; SEM image of nanowire deposited on PI film; simulation result of S_{11} variation; schematic depiction of effective dielectric constant (ε_{eff}) variation-based pressure sensing mechanism; relative capacitance variation of Ppy-coated porous PDMS according to pressure; SEM image of AFM tip coated with MXene; relative capacitance variation under continuous loading and unloading of pressure; mechanical property variation according to pore size; schematic illustration for discussion about linear relation between pressure and capacitance; relative capacitance variation under continuous loading and unloading of strain; S_{11} spectrum variation according to pressure using small pore based MXene-coated porous PDMS pressure sensor; S_{11} magnitude variation during 100 cycles of 30 kPa pressure loading and unloading; equivalent circuit model for analyzing relation between S_{11} and capacitance; resonant frequency variation during 100 cycles of 20% strain loading and unloading; schematic diagram of convolutional neural network architecture; predicted output values after training with 100 data and actual input values of test data; visualized simulation of magnetic flux induction on stacked 2D coils; S_{11} spectra variation at various distance or angles between the coil and the reader; visualized plot comparing the actual mechanical input and predicted one (PDF)

AUTHOR INFORMATION

Corresponding Authors

Sang Ouk Kim − *National Creative Research Initiative Center for Multi-dimensional Directed Nanoscale Assembly, Department of Materials Science and Engineering, KAIST Institute for Nanocentury, Korea Advanced Institute of Science and Technology (KAIST), Daejeon 34141, Republic of Korea*; Email: sangouk.kim@kaist.ac.kr

Steve Park − *Department of Materials Science and Engineering, Korea Advanced Institute of Science and Technology (KAIST), Daejeon 34141, Republic of Korea*; Email: stevepark@kaist.ac.kr

Authors

Gun-Hee Lee − *Department of Materials Science and Engineering, Korea Advanced Institute of Science and Technology (KAIST), Daejeon 34141, Republic of Korea*

Gang San Lee − *National Creative Research Initiative Center for Multi-dimensional Directed Nanoscale Assembly, Department of Materials Science and Engineering, KAIST Institute for Nanocentury, Korea Advanced Institute of Science and Technology (KAIST), Daejeon 34141, Republic of Korea*

Junyoung Byun − *School of Electrical Engineering, Korea Advanced Institute of Science and Technology (KAIST), Daejeon 34141, Republic of Korea*

Jun Chang Yang − *Department of Materials Science and Engineering, Korea Advanced Institute of Science and Technology (KAIST), Daejeon 34141, Republic of Korea*

Chorom Jang − *School of Electrical and Electronic Engineering, Yonsei University, Seoul 03722, Republic of Korea*

Seongrak Kim − *Department of Materials Science and Engineering, Korea Advanced Institute of Science and Technology (KAIST), Daejeon 34141, Republic of Korea*

Hyeonji Kim − *Department of Materials Science and Engineering, Korea Advanced Institute of Science and Technology (KAIST), Daejeon 34141, Republic of Korea*

Jin-Kwan Park − *School of Electrical and Electronic Engineering, Yonsei University, Seoul 03722, Republic of Korea*

Ho Jin Lee − *National Creative Research Initiative Center for Multi-dimensional Directed Nanoscale Assembly, Department of Materials Science and Engineering, KAIST Institute for Nanocentury, Korea Advanced Institute of Science and Technology (KAIST), Daejeon 34141, Republic of Korea*

Jong-Gwan Yook − *School of Electrical and Electronic Engineering, Yonsei University, Seoul 03722, Republic of Korea*

Complete contact information is available at: https://pubs.acs.org/10.1021/acsnano.0c05105

Author Contributions

G.-H.L. and G.S.L. contributed equally to this work. G.-H.L. designed and fabricated the wireless sensing system and performed sensor/device characterization. He also developed the deep learning-based monitoring platform. G.S.L. synthesized MXene, designed and fabricated the MXene-based sensor, and analyzed its characterization. J.B. implemented a deep learning algorithm. C.J. performed the computational simulation for the wireless sensing platform. S.O.K. and S.P. supervised the project. G.-H.L., G.S.L., S.O.K., and S.P. wrote the manuscript. All authors reviewed and commented on the manuscript.

Notes

The authors declare no competing financial interest.

ACKNOWLEDGMENTS

This work was supported by the National Research Foundation of Korea (NRF) grant funded by the Korea government (MSIT) (2019R1A5A8080326), KIST-KAIST Joint research lab (2V05750), National Creative Research Initiative (CRI) Center for Multi-Dimensional Directed Nanoscale Assembly (2015R1A3A2033061), and research

which has been conducted as part of the KAIST-funded Global Singularity Research Program for 2019. G.-H.L. was supported by the KAIST Venture Research Program for Graduate & Ph.D students.

REFERENCES

(1) Xie, Z. Q.; Avila, R.; Huang, Y. G.; Rogers, J. A. Flexible and Stretchable Antennas for Biointegrated Electronics. *Adv. Mater.* **2020**, *32*, 1902767.

(2) Park, Y. G.; Lee, S.; Park, J. U. Recent Progress in Wireless Sensors for Wearable Electronics. *Sensors* **2019**, *19*, 4353.

(3) Yang, J. C.; Mun, J.; Kwon, S. Y.; Park, S.; Bao, Z. N.; Park, S. Electronic Skin: Recent Progress and Future Prospects for Skin-Attachable Devices for Health Monitoring, Robotics, and Prosthetics. *Adv. Mater.* **2019**, *31*, 1970337.

(4) Boutry, C. M.; Beker, L.; Kaizawa, Y.; Vassos, C.; Tran, H.; Hinckley, A. C.; Pfattner, R.; Niu, S. M.; Li, J. H.; Claverie, J.; Wang, Z.; Chang, J.; Fox, P. M.; Bao, Z. N. Biodegradable and Flexible Arterial-Pulse Sensor for the Wireless Monitoring of Blood Flow. *Nat. Biomed. Eng.* **2019**, *3*, 47−57.

(5) Koo, J.; MacEwan, M. R.; Kang, S. K.; Won, S. M.; Stephen, M.; Gamble, P.; Xie, Z. Q.; Yan, Y.; Chen, Y. Y.; Shin, J.; Birenbaum, N.; Chung, S. J.; Kim, S. B.; Khalifeh, J.; Harburg, D. V.; Bean, K.; Paskett, M.; Kim, J.; Zohny, Z. S.; Lee, S. M.; et al. Wireless Bioresorbable Electronic System Enables Sustained Nonpharmacological Neuroregenerative Therapy. *Nat. Med.* **2018**, *24*, 1830.

(6) Lee, G. H.; Park, J. K.; Byun, J.; Yang, J. C.; Kwon, S. Y.; Kim, C.; Jang, C.; Sim, J. Y.; Yook, J. G.; Park, S. Parallel Signal Processing of a Wireless Pressure-Sensing Platform Combined with Machine-Learning-Based Cognition, Inspired by the Human Somatosensory System. *Adv. Mater.* **2020**, *32*, 1906269.

(7) Nie, B. Q.; Huang, R.; Yao, T.; Zhang, Y. Q.; Miao, Y. H.; Liu, C. R.; Liu, J.; Chen, X. J. Textile-Based Wireless Pressure Sensor Array for Human-Interactive Sensing. *Adv. Funct. Mater.* **2019**, *29*, 1808786.

(8) Niu, S. M.; Matsuhisa, N.; Beker, L.; Li, J. X.; Wang, S. H.; Wang, J. C.; Jiang, Y. W.; Yan, X. Z.; Yun, Y. J.; Burnett, W.; Poon, A. S. Y.; Tok, J. B. H.; Chen, X. D.; Bao, Z. N. A Wireless Body Area Sensor Network Based on Stretchable Passive Tags. *Nat. Electron.* **2019**, *2*, 361−368.

(9) Son, D.; Kang, J.; Vardoulis, O.; Kim, Y.; Matsuhisa, N.; Oh, J. Y.; To, J. W. F.; Mun, J. W.; Katsumata, T.; Liu, Y. X.; McGuire, A. F.; Krason, M.; Molina-Lopez, F.; Ham, J.; Kraft, U.; Lee, Y.; Yun, Y.; Tok, J. B. H.; Bao, Z. N. An Integrated Self-Healable Electronic Skin System Fabricated *via* Dynamic Reconstruction of a Nanostructured Conducting Network. *Nat. Nanotechnol.* **2018**, *13*, 1057−1065.

(10) Pozar, D. M. *Microwave Engineering*; John Wiley & Sons: Hoboken, NJ, 2009.

(11) Chortos, A.; Liu, J.; Bao, Z. A. Pursuing Prosthetic Electronic Skin. *Nat. Mater.* **2016**, *15*, 937−950.

(12) Dahiya, R.; Akinwande, D.; Chang, J. S. Flexible Electronic Skin: From Humanoids to Humans. *Proc. IEEE* **2019**, *107*, 2011−2015.

(13) Dahiya, R. S.; Metta, G.; Valle, M.; Sandini, G. Tactile Sensing-From Humans to Humanoids. *IEEE Trans. Robot.* **2010**, *26*, 1−20.

(14) Ha, M.; Lim, S.; Ko, H. Wearable and Flexible Sensors for User-Interactive Health-Monitoring Devices. *J. Mater. Chem. B* **2018**, *6*, 4043−4064.

(15) Yang, T. T.; Xie, D.; Li, Z. H.; Zhu, H. W. Recent Advances in Wearable Tactile Sensors: Materials, Sensing Mechanisms, and Device Performance. *Mater. Sci. Eng., R* **2017**, *115*, 1−37.

(16) Boutry, C. M.; Kaizawa, Y.; Schroeder, B. C.; Chortos, A.; Legrand, A.; Wang, Z.; Chang, J.; Fox, P.; Bao, Z. N. A Stretchable and Biodegradable Strain and Pressure Sensor for Orthopaedic Application. *Nat. Electron.* **2018**, *1*, 314−321.

(17) Courteny, T. H. *Mechanical Behavior of Materials*; Waveland Press: Long Grove, IL, 2005.

(18) Choi, S.; Yoon, K.; Lee, S.; Lee, H. J.; Lee, J.; Kim, D.; Kim, M. S.; Lee, T.; Pang, C. Conductive Hierarchical Hairy Fibers for Highly Sensitive, Stretchable, and Water-Resistant Multimodal Gesture-Distinguishable Sensor, VR Applications. *Adv. Funct. Mater.* **2019**, *29*, 1905808.

(19) Ge, J.; Sun, L.; Zhang, F. R.; Zhang, Y.; Shi, L. A.; Zhao, H. Y.; Zhu, H. W.; Jiang, H. L.; Yu, S. H. A Stretchable Electronic Fabric Artificial Skin with Pressure-, Lateral Strain-, and Flexion-Sensitive Properties. *Adv. Mater.* **2016**, *28*, 722−728.

(20) Park, S.; Kim, H.; Vosgueritchian, M.; Cheon, S.; Kim, H.; Koo, J. H.; Kim, T. R.; Lee, S.; Schwartz, G.; Chang, H.; Bao, Z. A. Stretchable Energy-Harvesting Tactile Electronic Skin Capable of Differentiating Multiple Mechanical Stimuli Modes. *Adv. Mater.* **2014**, *26*, 7324−7332.

(21) Hua, Q. L.; Sun, J. L.; Liu, H. T.; Bao, R. R.; Yu, R. M.; Zhai, J. Y.; Pan, C. F.; Wang, Z. L. Skin-Inspired Highly Stretchable and Conformable Matrix Networks for Multifunctional Sensing. *Nat. Commun.* **2018**, *9*, 244.

(22) Oh, J.; Yang, J. C.; Kim, J. O.; Park, H.; Kwon, S. Y.; Lee, S.; Sim, J. Y.; Oh, H. W.; Kim, J.; Park, S. Pressure Insensitive Strain Sensor with Facile Solution-Based Process for Tactile Sensing Applications. *ACS Nano* **2018**, *12*, 7546−7553.

(23) Yang, J. C.; Kim, J. O.; Oh, J.; Kwon, S. Y.; Sim, J. Y.; Kim, D. W.; Choi, H. B.; Park, S. Microstructured Porous Pyramid-Based Ultrahigh Sensitive Pressure Sensor Insensitive to Strain and Temperature. *ACS Appl. Mater. Interfaces* **2019**, *11*, 19472−19480.

(24) Shahzad, F.; Alhabeb, M.; Hatter, C. B.; Anasori, B.; Man Hong, S.; Koo, C. M.; Gogotsi, Y. Electromagnetic Interference Shielding with 2D Transition Metal Carbides (MXenes). *Science* **2016**, *353*, 1137−1140.

(25) Yun, T.; Kim, H.; Iqbal, A.; Cho, Y. S.; Lee, G. S.; Kim, M. K.; Kim, S. J.; Kim, D.; Gogotsi, Y.; Kim, S. O.; Koo, C. M. Electromagnetic Shielding of Monolayer MXene Assemblies. *Adv. Mater.* **2020**, *32*, 1906769.

(26) Tu, S. B.; Jiang, Q.; Zhang, X. X.; Alshareef, H. N. Large Dielectric Constant Enhancement in MXene Percolative Polymer Composites. *ACS Nano* **2018**, *12*, 3369−3377.

(27) Zhu, X. Y.; Xu, Q.; Li, H. K.; Liu, M. Y.; Li, Z. H.; Yang, K.; Zhao, J. W.; Qian, L.; Peng, Z. L.; Zhang, G. M.; Yang, J. J.; Wang, F.; Li, D. C.; Lan, H. B. Fabrication of High-Performance Silver Mesh for Transparent Glass Heaters *via* Electric-Field-Driven Microscale 3D Printing and UV-Assisted Microtransfer. *Adv. Mater.* **2019**, *31*, 1902479.

(28) Du, P.; Lin, X.; Zhang, X. Tunable Electrical and Mechanical Responses of PDMS and Polypyrrole Nanowire Composites. *J. Phys. D: Appl. Phys.* **2013**, *46*, 195303.

(29) Kim, I. H.; Yun, T.; Kim, J. E.; Yu, H.; Sasikala, S. P.; Lee, K. E.; Koo, S. H.; Hwang, H.; Jung, H. J.; Park, J. Y.; Jeong, H. S.; Kim, S. O. Mussel-Inspired Defect Engineering of Graphene Liquid Crystalline Fibers for Synergistic Enhancement of Mechanical Strength and Electrical Conductivity. *Adv. Mater.* **2018**, *30*, 1803267.

(30) Wang, H.; Lin, C. C.; Zhang, X. R.; Lin, K. L.; Wang, X. D.; Shen, S. G. Mussel-Inspired Polydopamine Coating: A General Strategy to Enhance Osteogenic Differentiation and Osseointegration for Diverse Implants. *ACS Appl. Mater. Interfaces* **2019**, *11*, 7615−7625.

(31) Kim, J. O.; Kwon, S. Y.; Kim, Y.; Choi, H. B.; Yang, J. C.; Oh, J.; Lee, H. S.; Sim, J. Y.; Ryu, S.; Park, S. Highly Ordered 3D Microstructure-Based Electronic Skin Capable of Differentiating Pressure, Temperature, and Proximity. *ACS Appl. Mater. Interfaces* **2019**, *11*, 1503−1511.

(32) Jang, C.; Park, J. K.; Lee, H. J.; Yun, G. H.; Yook, J. G. Temperature-Corrected Fluidic Glucose Sensor Based on Microwave Resonator. *Sensors* **2018**, *18*, 3850.

(33) Bengo, Y. *Learning Deep Architectures for AI*; Now Publishers: Hanover, MA, 2009.

(34) Han, S.; Pool, J.; Tran, J.; Dally, W. J. Learning Both Weights and Connections for Efficient Neural Networks. *Advances in Neural Information Processing Systems*; Neural Information Processing Systems (Nips): La Jolla, CA, 2015; Vol. 28.

https://dx.doi.org/10.1021/acsnano.0c05105
ACS Nano XXXX, XXX, XXX−XXX

(35) Yang, G.; Rothrauff, B. B.; Tuan, R. S. Tendon and Ligament Regeneration and Repair: Clinical Relevance and Developmental Paradigm. *Birth Defects Res., Part C* **2013**, *99*, 203−222.
(36) Ganin, Y.; Ustinova, E.; Ajakan, H.; Germain, P.; Larochelle, H.; Laviolette, F.; Marchand, M.; Lempitsky, V. Domain-Adversarial Training of Neural Networks. *J. Mach. Learn. Res.* **2016**, *17*, 35.
(37) Bae, G. Y.; Han, J. T.; Lee, G.; Lee, S.; Kim, S. W.; Park, S.; Kwon, J.; Jung, S.; Cho, K. Pressure/Temperature Sensing Bimodal Electronic Skin with Stimulus Discriminability and Linear Sensitivity. *Adv. Mater.* **2018**, *30*, 1803388.
(38) Jeong, C.; Lee, J. S.; Park, B.; Hong, C. S.; Kim, J. U.; Kim, T. I. Controllable Configuration of Sensing Band in a Pressure Sensor by Lenticular Pattern Deformation on Designated Electrodes. *Adv. Mater.* **2019**, *31*, 1902689.
(39) Lin, R.; Kim, H. J.; Achavananthadith, S.; Kurt, S. A.; Tan, S. C.; Yao, H.; Tee, B. C. K.; Lee, J. K. W.; Ho, J. S. Wireless Battery-Free Body Sensor Networks Using Near-Field-Enabled Clothing. *Nat. Commun.* **2020**, *11*, 444.

https://dx.doi.org/10.1021/acsnano.0c05105
ACS Nano XXXX, XXX, XXX−XXX